Title

Gating pore currents occur in CaV1.1 domain III mutants associated with HypoPP.

Journal

Journal of General Physiology, 153(11)

Authors

Wu, Fenfen
Quinonez, Marbella
Cannon, Stephen

Publication Date

2021-11-01

DOI

10.1085/jgp.202112946

Peer reviewed

JGP Journal of General Physiology

ARTICLE

Gating pore currents occur in $Ca_V1.1$ domain III mutants associated with HypoPP

Fenfen Wu, Marbella Quinonez, and Stephen C. Cannon[a]

Mutations in the voltage sensor domain (VSD) of $Ca_V1.1$, the α_{1S} subunit of the L-type calcium channel in skeletal muscle, are an established cause of hypokalemic periodic paralysis (HypoPP). Of the 10 reported mutations, 9 are missense substitutions of outer arginine residues (R1 or R2) in the S4 transmembrane segments of the homologous domain II, III (DIII), or IV. The prevailing view is that R/X mutations create an anomalous ion conduction pathway in the VSD, and this so-called gating pore current is the basis for paradoxical depolarization of the resting potential and weakness in low potassium for HypoPP fibers. Gating pore currents have been observed for four of the five $Ca_V1.1$ HypoPP mutant channels studied to date, the one exception being the charge-conserving R897K in R1 of DIII. We tested whether gating pore currents are detectable for the other three HypoPP $Ca_V1.1$ mutations in DIII. For the less conserved R1 mutation, R897S, gating pore currents with exceptionally large amplitude were observed, correlating with the severe clinical phenotype of these patients. At the R2 residue, gating pore currents were detected for R900G but not R900S. These findings show that gating pore currents may occur with missense mutations at R1 or R2 in S4 of DIII and that the magnitude of this anomalous inward current is mutation specific.

Introduction

Hypokalemic periodic paralysis (HypoPP) is an inherited disorder of skeletal muscle in which recurrent episodes of weakness occur in association with low extracellular $[K^+]$, <3 mM (normal range 3.5–5.5 mM; Cannon, 2015). During an attack, the resting potential is paradoxically depolarized, and this sustained depolarization inactivates sodium channels, thereby reducing fiber excitability and causing weakness. The molecular basis for HypoPP is heterogeneous, with missense mutations in the pore-forming α_{1S} subunit of the voltage-gated L-type Ca^{2+} channel ($Ca_V1.1$) accounting for ∼60% of cases and missense mutations in the α subunit of $Na_V1.4$ occurring in another 20% (Sternberg et al., 2001). Remarkably, 9 of 10 established HypoPP mutations in $Ca_V1.1$ and all 13 in $Na_V1.4$ are missense mutations at arginine residues in the outer positions (R1 or R2) of S4 transmembrane segments in the voltage sensor domains (VSDs; Cannon, 2017; Matthews et al., 2009).

The conserved structural motif of HypoPP mutations has an accompanying commonality of functional defects. Scanning mutagenesis studies, originally designed to map voltage-dependent movement of S4 segments in voltage-gated K^+ (K_V) channels, revealed the surprising finding that R/X mutations may create an anomalous leakage current in the VSD (Starace and Bezanilla, 2001; Tombola et al., 2005). When R1 or R2 is mutated, ion conduction through this "gating pore" is permissive at hyperpolarized potentials when the S4 is in the inward or "down" conformation and the R1 or R2 residue lies near the hydrophobic charge transfer center (CTC) of the VSD. Depolarization favors outward movement of S4, which removes the R/X mutation from the critical hydrophobic CTC, and the anomalous gating pore becomes nonconducting (Monteleone et al., 2017; Moreau et al., 2014). This insight directly led to the hypothesis that R/X mutations in HypoPP might also give rise to gating pore currents and that this would produce an anomalous inward current at the resting potential of muscle fibers. This notion was quickly confirmed for HypoPP mutations in $Na_V1.4$ (Sokolov et al., 2007; Struyk and Cannon, 2007) and was subsequently verified for 12 of 13 R/X mutations in $Na_V1.4$, with the one exception being the only known charge-conserving mutation, R219K (Kubota et al., 2020). Moreover, model simulations show that the small anomalous conductance of the gating pore current (only ∼1% of the total resting conductance in a muscle fiber) is sufficient to cause paradoxical depolarization of the resting potential in low K^+ (Jurkat-Rott et al., 2012; Struyk and Cannon, 2008).

Department of Physiology, David Geffen School of Medicine, University of California, Los Angeles, Los Angeles CA.

Correspondence to Stephen C. Cannon: sccannon@mednet.ucla.edu.

Confirmation that HypoPP R/X mutations in S4 segments of $Ca_V1.1$ are also permissive for gating pore currents, I_{gp}, lagged behind the studies of $Na_V1.4$. This delay occurred because in heterologous systems $Ca_V1.1$ does not express well at the plasma membrane, and high levels of expression are required for sufficient signal to noise to detect I_{gp}. In a knock-in mutant mouse model of $Ca_V1.1$-R528H HypoPP, but not in WT, we observed an aberrant inward current that was not blocked by dihydropyridines, tetrodotoxin, TEA, 4-aminopyridine, or 9-anthracenecarboxylic acid, consistent with a gating pore current (Wu et al., 2012). Expression of HypoPP $Ca_V1.1$ mutant constructs by electroporation of muscle fibers in vivo also showed evidence of an anomalous inward current consistent with I_{gp} for R1239H (Fuster et al., 2017a) and the atypical mutation V876E in domain III (DIII) S3 (Fuster et al., 2017b), which is the only well-established example of a HypoPP mutation that is not R/X in S4. The detection of I_{gp} was technically challenging for all of these studies in mouse muscle fibers because it is difficult to sufficiently block all of the endogenous conductances to clearly observe the gating pore current. For example, the evidence for I_{gp} in the electroporation studies was based on a 20% increase of the inward current compared with WT and required a large sample size of ∼20 fibers to detect this difference. Currently, no specific blockers of I_{gp} with sufficient potency have been identified that would enable a pharmacologic leak subtraction strategy to isolate the gating pore current.

More recently, an accessory protein, Stac3, was identified (Horstick et al., 2013; Nelson et al., 2013) that is essential for skeletal muscle–type excitation–contraction coupling and that greatly enhances expression of $Ca_V1.1$ at the plasma membrane (Polster et al., 2015). We showed that Stac3 coexpression with L-type Ca^{2+} channel subunits in *Xenopus laevis* oocytes dramatically increases Ca^{2+} current by 100-fold (Wu et al., 2018) and achieves sufficient channel levels to detect gating pore currents for the $Ca_V1.1$ HypoPP mutations in DII (R528H and R528G). Four HypoPP mutations have been reported in DIII of $Ca_V1.1$ (R897S, R897K, R900G, and R900S). In a collaborative study, we recently showed that the atypical charge-conserving mutation at R1 in DIII, R897K, does not lead to a gating pore current detectable in the oocyte expression study (Kubota et al., 2020). In the present study, we ascertained whether gating pore currents are detectable for the other three $Ca_V1.1$ HypoPP mutations in DIII. Of note, the R897S mutation is associated with a severe clinical phenotype (Chabrier et al., 2008; Hanchard et al., 2013), and we found the largest amplitude I_{gp} encountered for any HypoPP mutant channel ($Na_V1.4$ or $Ca_V1.1$), even though the charge-conserving mutation at the same residue, R897K, had no detectable I_{gp}. Similarly, at the R2 position in DIII, the gating pore current was detected for R900G but not for substitution of the larger residue R900S.

Materials and methods

Expression of human $Ca_V1.1$ ($hCa_V1.1$) channels in oocytes

The human α_{1S} subunit of the skeletal muscle Ca^{2+} channel was expressed in *Xenopus* oocytes as previously described (Wu et al., 2018). Briefly, the $hCa_V1.1$, rabbit β_{1a}, and mouse Stac3 cDNAs were subcloned into an oocyte-optimized expression vector, pGEMHE (Liman et al., 1992), whereas the rat α_2-δ_{1b} cDNA was inserted into pcDNA3 (Invitrogen). Site-directed mutagenesis of $hCa_V1.1$ was performed using the QuikChange II Mutagenesis Kit (Agilent) to create the HypoPP missense mutations R897S, R900G, and R900S, verified by sequencing the entire cDNA insert and flanking regions. Complementary RNA was synthesized by in vitro transcription (∼2 ng/nl) using the mMESSAGE mMACHINE kit (Ambion).

Oocytes were harvested by partial oophorectomy and defolliculated in collagenase type I at room temperature for 2 h. Equal volumes of all four transcripts ($hCa_V1.1$, β_{1b}, α_2-δ_{1b}, and Stac3) were combined in a master mix, and 50 nl was injected into the animal pole of each oocyte. Oocytes were maintained at 18°C in 0.5× Leibovitz's L-15 medium (HyClone) supplemented with 1% horse serum, 100 U/ml penicillin, 100 µg/ml streptomycin, and 100 µg/ml amikacin. All experiments were performed within the guidelines established by the University of California, Los Angeles, Institutional Animal Care and Use Committee.

Electrophysiology

Currents were recorded 3–6 d after RNA injections using the cut-open oocyte voltage clamp in headstage mode (Dagan CA-1B) as previously described (Wu et al., 2018). After mounting the oocyte in the recording chamber, the membrane exposed to the bottom compartment was permeabilized by brief application of 0.1% saponin. A voltage-sensing microelectrode was inserted into the dome of the oocyte protruding into the upper compartment. The upper and middle compartments were actively clamped using platinum wire-threaded salt bridges filled with Cl^- free agar (1 M sodium methanesulfonate and 10 mM HEPES, pH 7.0). The linear membrane capacitance was compensated with the analogue circuitry of the amplifier, but no offset or linear leak subtraction was performed. Currents were low-pass filtered at 10 kHz to measure gating charge displacement and at 1 kHz for measuring ionic currents. Signals were sampled at 20 kHz with 16-bit resolution.

Chloride-free solutions were used for all recordings to minimize the contribution from endogenous chloride conductances in the oocyte. Prior to mounting the oocyte in the recording chamber, oocytes were injected with 100 nl of a BAPTA solution (100 mM BAPTA-K_4 and 10 HEPES, pH 7.0 with Mes) to buffer intracellular Ca^{2+} and further reduce endogenous Ca^{2+}-activated Cl^- currents. The internal solution (bottom compartment) contained 96 mM KOH and 10 mM HEPES adjusted to pH 7.0 with methanesulfonic acid. The standard external solution used for the middle (guard) and upper compartments contained (in mM): 96 NaOH, 6 calcium acetate, 10 HEPES, and 0.1 ouabain titrated to pH 7.0 with methanesulfonic acid. For measurement of ionic current conducted by the main pore of the $Ca_V1.1$ subunit, the Ca^{2+} of the external solution was replaced by 10 mM barium acetate. Gating charge-displacement currents were measured by substituting 2 mM Co^{2+} for Ca^{2+} in the external solution to block conduction by the pore. For studies of the permeation properties of the gating pore current, the external Na^+ was replaced by 110 mM NMDG (see Fig. 7) or a mixture of 60 mM NMDG and 60 mM guanidinium (see Fig. 9). Block by divalent cations (see Fig. 8) was assessed by bath exchange of the top compartment

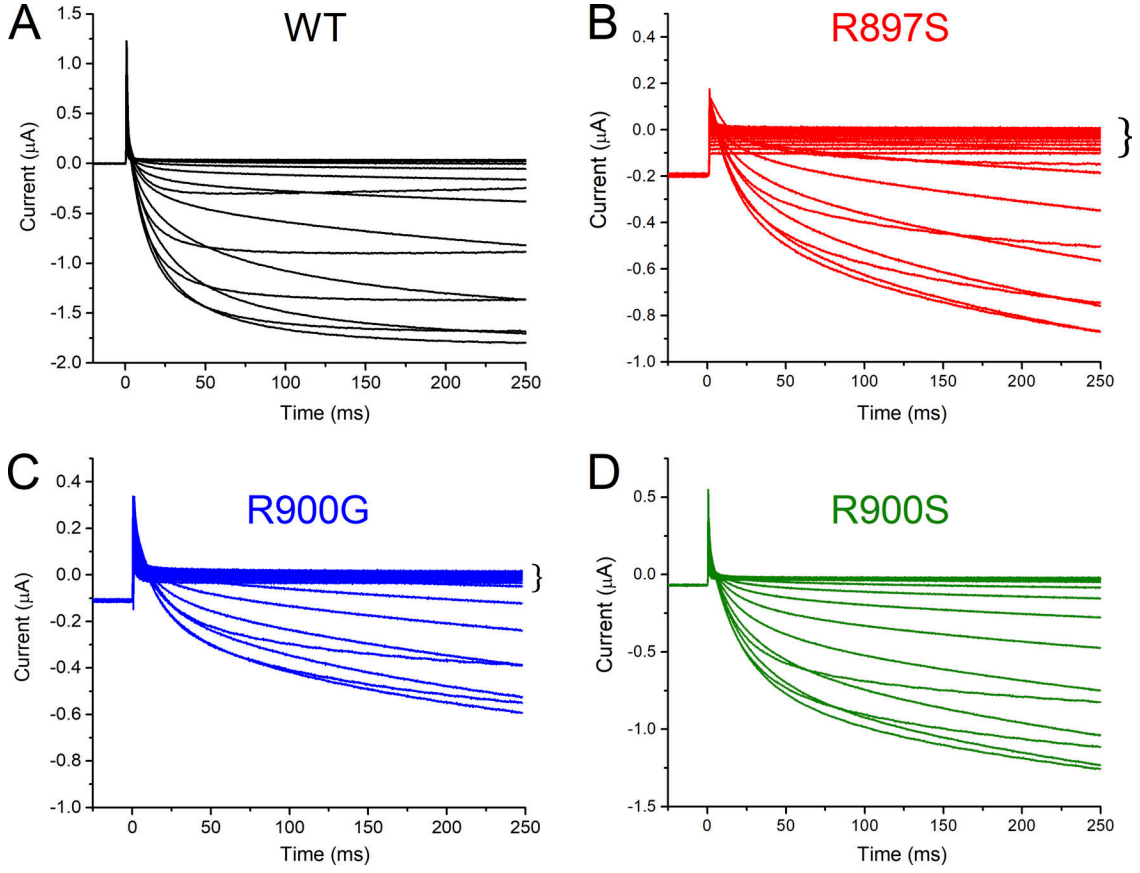

Figure 1. **Ba^{2+} currents conducted by WT and mutant $hCa_V1.1$ channels. (A–D)** Currents were recorded for step depolarizations from −50 mV to +40 mV in 5-mV increments from a holding potential of −100 mV in oocytes expressing WT (A), R897S (B), R900G (C), or R900S (D) $hCa_V1.1$ subunits. Neither leak nor offset subtraction was performed.

from a control with 6 mM Ca^{2+} to test solutions with 4 mM Ca^{2+} and 2 mM of either Ba^{2+} or Co^{2+}.

Data analysis

The peak I-V relation for the Ba^{2+} currents was fit to an ohmic conductance that was scaled by a Boltzmann function to model the voltage dependence of channel activation:

$$I_{Ba} = G_{max}(V - E_{rev})/[1 + e^{-(V-V_{1/2})/k}],$$

where G_{max} is the maximal conductance, E_{rev} is the fitted reversal potential, $V_{1/2}$ is the voltage midpoint for activation, and k is the steepness factor. The inward Ba^{2+} current increased monotonically with time (see Figs. 1 and 3 A), and although the time course was more complex than a single exponential, we used a single exponential fit to compute an apparent time constant because this approach of using a single number facilitates the comparison between WT and HypoPP mutant channels. A more exact fit using a double exponential showed that ∼80% of the response can be accounted for by a single exponential component. A qualitative comparison was also performed by amplitude scaling of the currents to the maximum value and superimposing the traces (see Fig. 3 A).

The "on" gating charge, $Q(V)$, was calculated as the area under the charge-displacement current elicited by a voltage step from −100 mV. Most of the linear capacitance of the membrane

Table 1. **Voltage dependence of channel activation**

$hCa_V1.1$ construct	I_{peak} (μA)	$V_{1/2}$ (mV)	k (mV)	G_{max} (μS)	E_{rev} (mV)
WT (n = 8)[a]	−1.6 ± 0.16	16 ± 1.4	6.8 ± 0.34	78 ± 9.2	52 ± 2.0
R897S (n = 6)	−0.67 ± 0.082[b]	19 ± 1.1	7.9 ± 0.34[b]	49 ± 4.5[b]	46 ± 2.0
R900G (n = 4)	−0.66 ± 0.028[b]	24 ± 1.0[b]	7.2 ± 0.06	52 ± 4.0[b]	49 ± 2.7
R900S (n = 8)	−1.1 ± 0.043[b]	17 ± 0.98	6.7 ± 0.12	60 ± 4.3[b]	49 ± 1.7

[a]Data reproduced from Wu et al., 2018.
[b]$P < 0.05$ compared with WT (ANOVA).

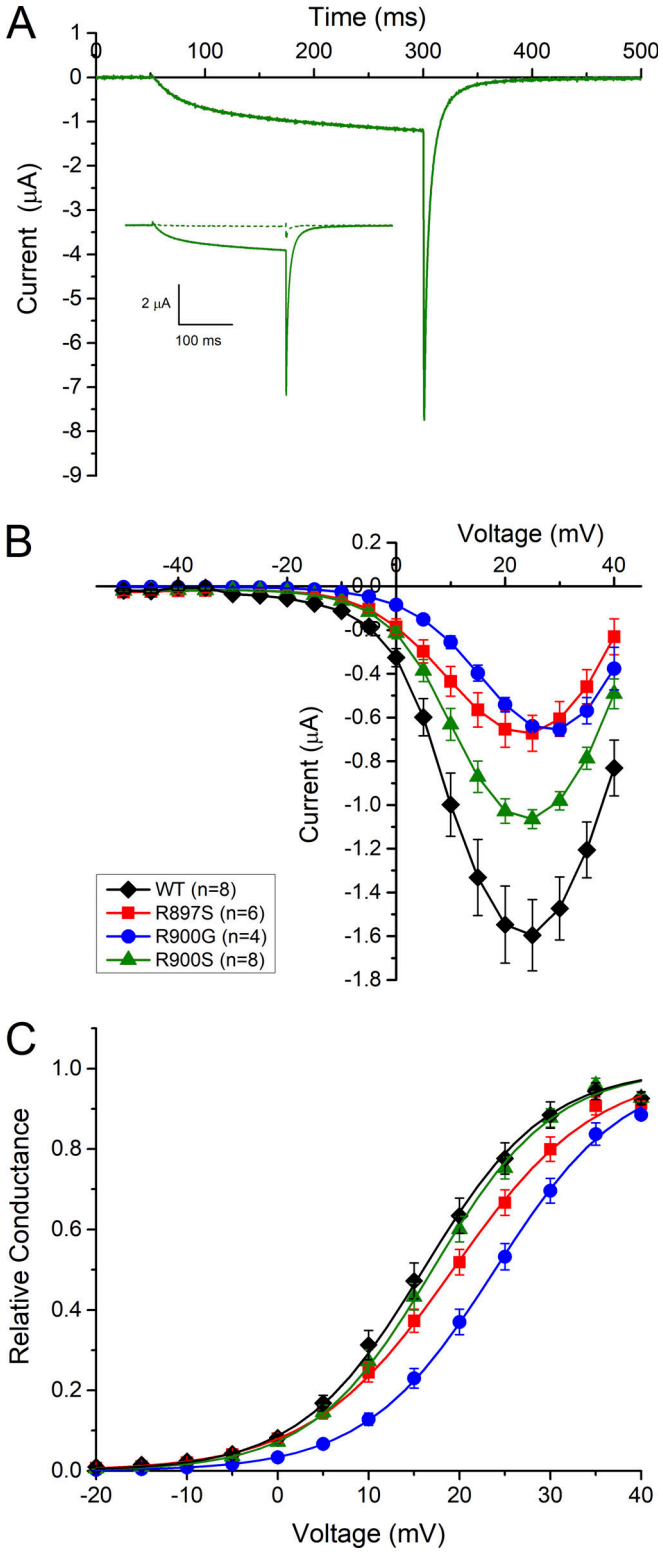

Figure 2. **Voltage-dependent activation of hCa$_V$1.1 channels. (A)** Most of the current recorded in 10 mM Ba^{2+} was conducted by hCa$_V$1.1 channels, as shown in this example for a voltage step to +25 mV in an oocyte expressing the R900S mutant. Inset shows the current in control (solid line) and then in a blocking solution with 10 μM nifedipine + 2 mM Co^{2+} (dashed line). The full-size plot shows the blocker-sensitive Ba^{2+} current. **(B)** The I-V relationship shows that the Ba^{2+} currents were of lower amplitude for all mutant channels than for WT. **(C)** The depolarized shift of activation for R900G mutant channels is shown more clearly in the plot of relative conductance. Symbols in B and C show the mean values (± SEM), and the curves show the Boltzmann fit using the mean values of the parameters. Error bars indicate the SEM.

was compensated by the analogue circuitry of the Dagan CA-1B, and the residual linear capacitance and nonspecific leakage current were compensated by subtracting a scaled version of the passive linear response for a depolarization from −100 mV to −80 mV. Secondary offset subtraction of the current 5 ms after the voltage step was used to compensate for potential effects from a nonlinear gating pore current, as previously described (Mi et al., 2014). The $Q(V)$ relation was fit to a Boltzmann distribution:

$$Q_{on} = Q_{max}/[1 + e^{-(V-V_{1/2})/k}],$$

where Q_{max} is the maximal Q_{on}, $V_{1/2}$ is the voltage at which half the charge has moved, and k is the steepness factor.

The detection of gating pore currents was optimized by measuring the isochronal current over the interval 5–8 ms, as done in our previous study of VSDII HypoPP mutant channels (Wu et al., 2018). This delay allows the gating charge-displacement current to decay back to 0 nA and at the same time is fast compared with the opening of the channel pore such that the majority of the ionic current is conducted by the gaiting pore (plus nonspecific leakage).

In all figures, the error bars indicate the SEM. Statistical tests for the difference between the mean values for parameter estimates of four constructs (WT and three HypoPP mutants) were assessed by two-tailed ANOVA with Bonferroni correction.

A simulation is provided in the supplemental text at the end of the PDF to show the feasibility of and potential sources of error for measuring charge displacement in the presence of a large-amplitude gating pore current.

Online supplemental material

Fig. S1 shows simulated currents produced by the sum of leak (I_{leak}), gating pore (I_{gp}), and charge-displacement components (I_q). Fig. S2 shows simulated $Q(V)$ curves. Table S1 lists model parameters. Supplemental text provides a numerical simulation to demonstrate the feasibility of estimating the gating charge displacement, based on conventional P/N leak-subtracted responses, despite the presence of a contribution from the nonlinear, voltage-dependent gating pore current.

Results

HypoPP DIII mutant channels are expressed in the plasma membrane and conduct Ba^{2+}

Ionic currents were recorded in the cut-open oocyte configuration with 10 mM external Ba^{2+} as the charge carrier and no added Ca^{2+}. Large-amplitude, slowly activating inward currents were observed at test potentials more positive than 0 mV for oocytes expressing WT and all three HypoPP mutant constructs (Fig. 1). The linear capacitive transient has been suppressed by analogue compensation of the amplifier, but otherwise these

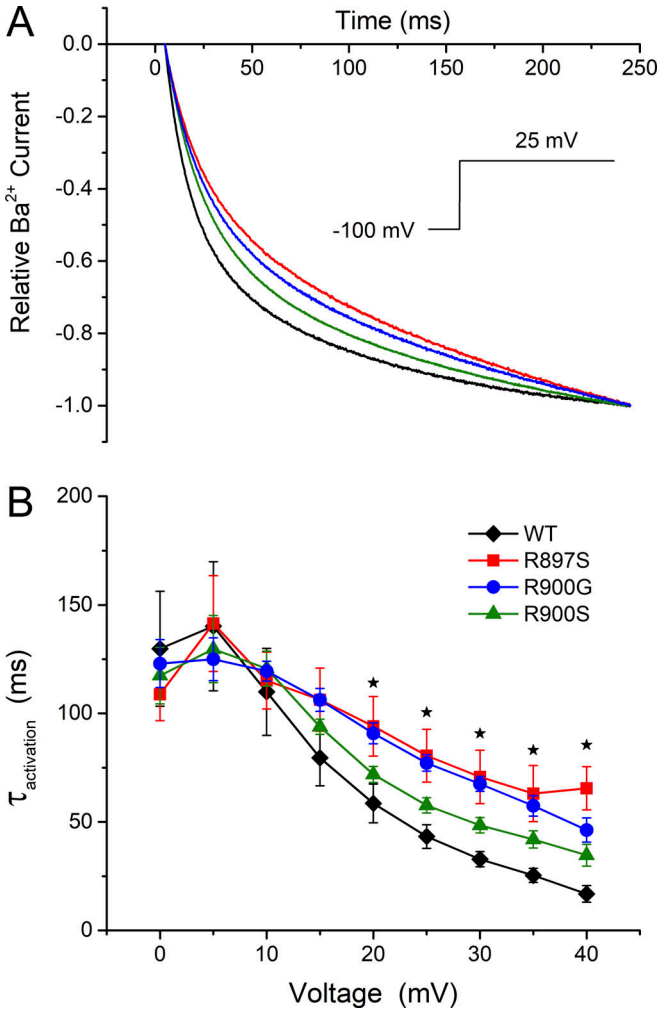

Figure 3. **Kinetics of activation for WT and HypoPP hCa$_V$1.1 channels.** **(A)** The time course for Ba^{2+} current activation is shown by superposition of amplitude-normalized currents elicited by a voltage step to +25 mV. For each response, the zero offset was set to the current value at 5 ms to allow time for relaxation of any residual uncompensated capacitance transient. The maximum current was set to the value at 240 ms after the start of the voltage step. The traces are average values for WT (n = 6), R897S (n = 5), R900G (n = 4), and R900S (n = 4). The SEM at each point in time was on the order of 0.01–0.03, which is barely distinguishable from the line for the mean value and has been omitted for clarity. **(B)** The time constant from a single exponential fit to the Ba^{2+} current is shown as a function of voltage step potential. The stars indicate the voltage range over which the mean values for R897S and R900G were larger than for WT (ANOVA; $P < 0.01$). Error bars indicate the SEM.

traces show currents without linear leak or offset subtraction. At the holding potential of −100 mV, an inward holding current was consistently larger for the R897S and R900G constructs than for WT or R900S, as shown in Fig. 1. The current amplitudes for test potentials from −50 to −10 mV spanned a larger range for R897S and R900G (e.g., curly bracket in Fig. 1, B and C) than for WT or R900S. These differences reflect a larger conductance in a voltage range below the activation of hCa$_V$1.1 channels for oocytes expressing R897S and R900G. This aberrant conductance in R897S and R900G mutant channels is the gating pore, and the anomalous currents are large enough to be detected compared with the Ba^{2+} current conducted by the central pore of hCa$_V$1.1.

Current conducted by the hCa$_V$1.1 pore was isolated as the component of the total current that was blocked by a combination of 10 µM nifedipine plus 2 mM Co^{2+}. Fig. 2 A shows an example of the nifedipine/Co^{2+}-sensitive current elicited by a test pulse to +25 mV in an oocyte expressing the R900S construct. Most of the total current was conducted by the hCa$_V$1.1 pore, as shown in the inset by the comparison of the current without blockers (solid line) and with blockers (dashed line). The I-V relation, measured as the nifedipine/Co^{2+}-sensitive current at the end of a 250-ms pulse, shows the current amplitude was smaller for HypoPP mutant constructs than for WT (Fig. 2 B). On average, the peak inward current amplitude was 42%, 41%, and 67% of WT for R897S, R900G, and R900S, respectively (Table 1, G_{max} values).

The voltage dependence of activation for I_{Ba} was shifted by 8 mV in the depolarized direction for R900G, whereas the voltage midpoint was not statistically different from WT for R897S or R900S (Fig. 2 C and Table 1). Although all three HypoPP mutations neutralize a gating charge in the DIII VSD, only the R897S mutation in the outermost R1 position decreased the slope of the G-V relation (k = 7.9 ± 0.34 mV compared with 6.8 ± 0.34 in WT).

The Ba^{2+} currents for the representative cells shown in Fig. 1 have slower activation kinetics for all three HypoPP mutant channels than for WT. This difference was consistently observed, as shown by superposition for the averages of amplitude-normalized Ba^{2+} currents elicited by a voltage step to 25 mV (Fig. 3 A). To quantitatively compare this difference, we fit the rising phase of the Ba^{2+} current with a single exponential, which accounts for ∼80% of this monotonically increasing transient. This approximation facilitates the comparison with a single activation time constant (τ_{act}). The rate of activation was approximately twofold slower for R897S and R900G mutant channels than for WT (20–40-mV range; ANOVA $P < 0.01$), whereas for R900S, the 1.5-fold slower trend was not statistically different from WT (Fig. 3 B).

We measured the gating charge displacement as an index of channel expression level at the membrane and to assess the voltage dependence for displacement of the voltage sensor. The inward rectification of gating pore currents produces a nonlinearity that may corrupt the standard P/N linear leak subtraction method used to isolate the charge-displacement current. We previously showed that secondary offset subtraction of the steady-state current (after the charge-displacement transient has decayed) can be used to compensate for this distortion (Mi et al., 2014). For those data, the amplitude of the gating pore current was ∼5% of the peak charge-displacement transient, and the estimated uncertainty for Q_{max} was ±7.5%. For R897S, however, the amplitude of the gating pore current was much larger (Fig. 1 B), and consequently the effect on P/N leak subtraction was much greater. Fig. 4 A shows representative current transients, without leak or offset subtraction, that were used to determine $Q(V)$ for R897S. The corresponding "leak trace" for a small voltage step from −100 mV to −80 mV is shown in Fig. 4 B. The conductance is rather large (150 nA/20 mV) because of contributions from both the "open" gating pore and the nonspecific leakage current. When strongly depolarized voltage

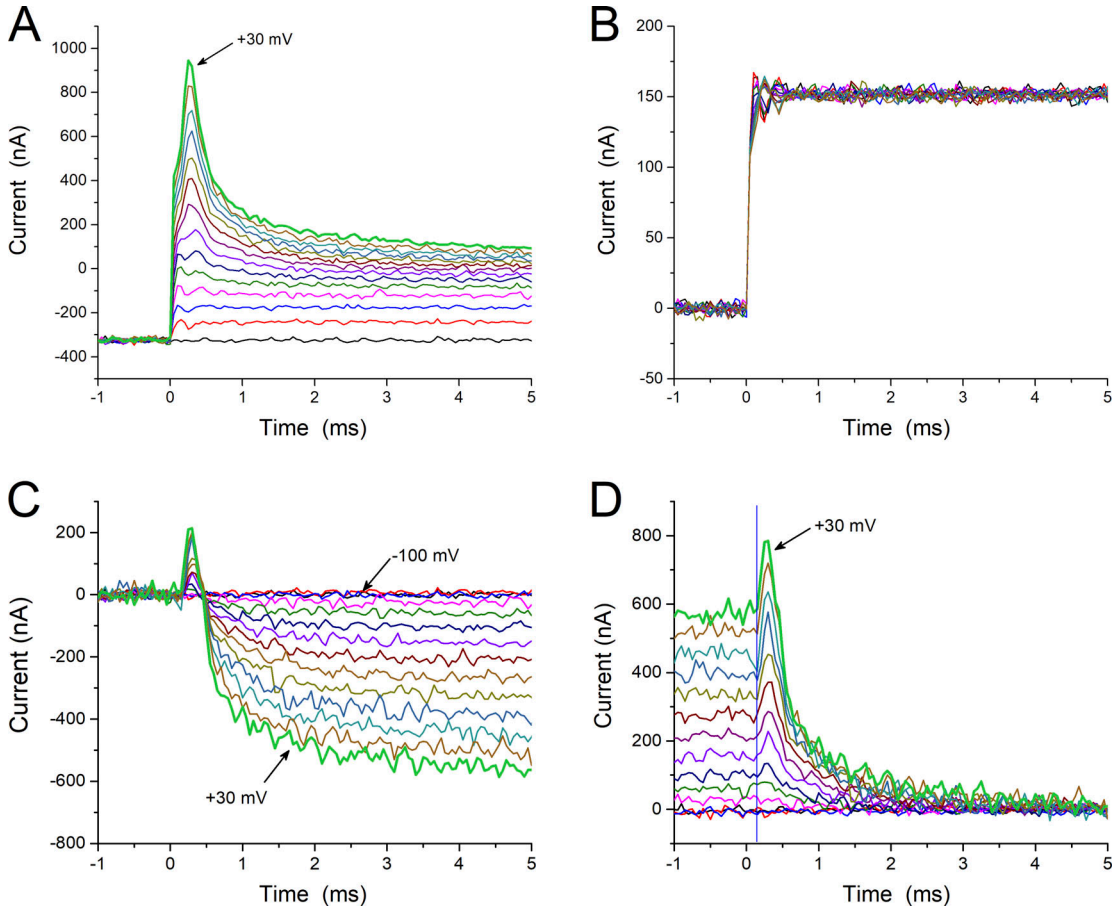

Figure 4. **Detection of charge-displacement currents in the presence of a large-amplitude nonlinear gating pore current for R897S. (A)** Currents elicited by depolarizations from −100 mV to +30 mV in 10-mV increments from an oocyte expressing R897S. No offset or leak subtraction has been performed. The capacitance compensation of the amplifier was used to cancel the linear capacitance of the oocyte membrane. **(B)** Superposition of currents recorded from leak pulses (−100 mV to −80 mV) applied between each of the trials in A. The baseline current ($t < 0$ *ms*) was approximately −325 nA, as shown in A, and has been digitally subtracted from each trace. **(C)** Baseline-subtracted currents from A are replotted after linearly scaled subtraction for the "leak" response in B. The scale factor for each trace is $\Delta V/20$ because the "leak" response was measured for a 20-mV depolarization. **(D)** Secondary offset subtraction of the steady-state current at 5 ms for the currents in A was performed to isolate the current transient that is primarily composed of the gating charge-displacement current (see supplemental text at the end of the PDF). The gating charge was calculated as the integral of the current for $t > 50$ µs, as shown by the vertical line.

steps were applied to measure charge displacement, the gating pore closed, so the linearly scaled P/N subtraction erroneously overcompensated and caused a substantial negative current in steady state (Fig. 4 C, at 5 ms). A secondary offset subtraction of this steady-state current was performed to derive the transient response that was integrated to calculate Q (Fig. 4 D).

Using this method, the maximal charge displacement, Q_{max}, was half that of WT for all three HypoPP mutant constructs (Fig. 5 A; $P < 0.001$). A commensurate decrease was observed in the peak Ba^{2+} current (Fig. 2), consistent with the notion that the expression of functional channels in the membrane for all three HypoPP mutant constructs was about half of that for WT. A plot of the relative charge displacement as a function of membrane potential showed a 21-mV leftward shift for oocytes expressing R897S compared with all other constructs (Fig. 5 B and Table 2). Neutralization of a gating charge (R1 or R2) in DIII did not reduce the slope of the $Q(V)$ curve compared with WT.

We performed model simulations (see supplemental text and Table S1) to estimate the possible error in determining $Q(V)$ that may have been introduced by residual effects of the nonlinear gating pore current, especially for R897S. In the limit, if the rate of gating pore closure is instantaneous, then there is no error. On the other hand, the slowest possible rate for closure of the gating pore would be with the same kinetics as the decay for the total charge displacement (movement of S4 is expected to directly close the gating pore, with no delay from allosteric coupling). In this slowest possible case, the contribution to the transient from the gating pore current would cause the amplitude of the apparent $Q(V)$ curve to be overestimated and to increase linearly at strongly depolarized potentials (Fig. S1 and Fig. S2). However, the $Q(V)$ for R897S in Fig. 5 B showed a clear plateau, suggesting that the gating pore does indeed close faster than the rate of decay for the charge displacement, and therefore our estimate for Q_{max} is reasonable. Importantly, over the entire range of simulated gating pore closing rates, the apparent voltage midpoint of $Q(V)$ did not have a leftward shift (Fig. S2 B). Therefore, we interpret the 21-mV leftward shift in Fig. 5 B to be an intrinsic feature of

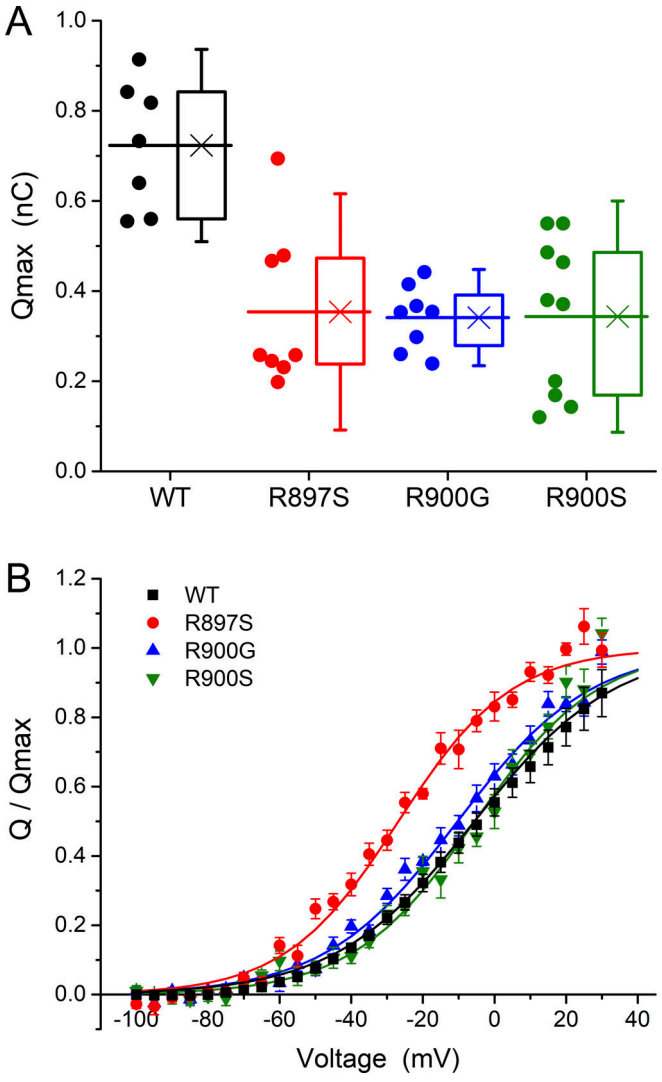

Figure 5. **Gating charge-displacement current was leftward shifted for R897S. (A)** Box plot shows the mean values (line), 25–75% interquartile (box), and SD (whiskers) for the maximum charge displacement observed in each oocyte. The Q_{max} for WT was larger (ANOVA; P < 0.001) than for any HypoPP mutant constructs, which were statistically indistinguishable. **(B)** The voltage dependence of relative charge displacement showed a leftward shift of 21 mV for R897S compared with WT (ANOVA; P < 0.001).

R897S gating and not an artifact of the method used to calculate charge displacement.

Gating pore currents were detected for R897S and R900G

The protocol we previously developed to detect gating pore currents for hCa$_V$1.1 DII HypoPP mutant channels (Wu et al., 2018) was used to test for detectable I_{GP} in the DIII HypoPP mutants. Voltage steps were applied from a holding potential of −100 mV, and most of the capacitive current was compensated by the analogue circuitry of the amplifier. No offset or linear leak subtraction was performed. The representative responses in Fig. 6 A show a larger holding current of −200 to −400 nA at V_{hold} = −100 mV for R900G and R897S compared with WT or R900S hCa$_V$1.1 (approximately −100 nA). These larger holding currents for R897S and R900G were associated with a higher

Table 2. **Gating charge displacement**

hCa$_V$1.1 construct	Q_{max} (nC)	$V_{1/2}$ (mV)	k (mV)
WT (n = 8)[a]	0.69 ± 0.060	−5.6 ± 1.5	19 ± 0.61
R897S (n = 8)	0.35 ± 0.062[b]	−27 ± 1.9[b]	16 ± 0.70[c]
R900G (n = 8)	0.34 ± 0.028[b]	−10 ± 1.7	19 ± 1.1
R900S (n = 10)	0.34 ± 0.054[b]	−5.5 ± 1.6	17 ± 0.93

[a]Data reproduced from Wu et al., 2018.
[b]P < 0.001 compared with WT (ANOVA).
[c]P < 0.05 compared with WT (ANOVA).

conductance (i.e., wider spread of ionic current levels) over the voltage range from −140 mV to −40 mV, which is hyperpolarized relative to activation of the Ba^{2+} current conducted by the pore of hCa$_V$1.1 (Fig. 2). Moreover, the response for R897S shows clear evidence for inward rectification (Fig. 6 A). These features are consistent with an anomalous gating pore current, I_{GP}, for R897S and R900G HypoPP mutant channels.

To quantify I_{GP}, we determined the time-averaged current over the interval 5–8 ms, which is late enough for the residual capacitive and charge-displacement currents to settle and is too early for activation of the Ba^{2+} current conducted by the main pore of hCa$_V$1.1 for V_{step} <10 mV. Average values for this isochronal current are plotted as a function of V_{step} in Fig. 6 B. The plots diverge at hyperpolarized potentials, with strong inward rectification for R897S and a clear separation from WT for R900G (P < 0.05 for V_{step} less than or equal to −85 mV). The measured current is a combination of nonspecific leakage current and I_{GP}. Because effective blockers have not been identified for I_{GP} in S4 R/X missense mutants of Ca$_V$, Na$_V$, or K$_v$ channels, it is not possible to pharmacologically separate I_{GP} from the total current. Moreover, a post hoc linear subtraction of the leak component, used to extract the inwardly rectifying I_{GP} for S4 R/X mutations in Na$_V$ (Sokolov et al., 2007; Struyk and Cannon, 2007), is not feasible for hCa$_V$1.1, because I_{GP} is usually linear (e.g., R528H and R528G in DII [Wu et al., 2018] and R900G herein). The gating pore current observed for R897S is remarkable because it is the only example of an hCa$_V$1.1 HypoPP mutation where I_{GP} shows strong inward rectification and because the amplitude is unusually large. The magnitude of the gating pore effect shown for R900G in Fig. 6 B is more typical for HypoPP hCa$_V$1.1 mutant channels studied in the oocyte expression system. For example, in our prior study of R528H and R528G in DII (Wu et al., 2018), the total inward current at hyperpolarized potentials (nonspecific leak plus I_{GP}) was approximately twice the amplitude of that observed for WT hCa$_V$1.1. For a DIV HypoPP mutation (R1239H) and the atypical mutation in S3 of DIII (V876E), the total inward current was only ∼40% larger than for WT when studied by plasmid electroporation into muscle of normal mice (Fuster et al., 2017a; Fuster et al., 2017b).

Permeation of the gating pore in DIII HypoPP hCa$_V$1.1

Permeation through an anomalous gating pore is variable and mutation specific. Gating pore currents may be either nonselective for monovalent cations or proton selective (especially for

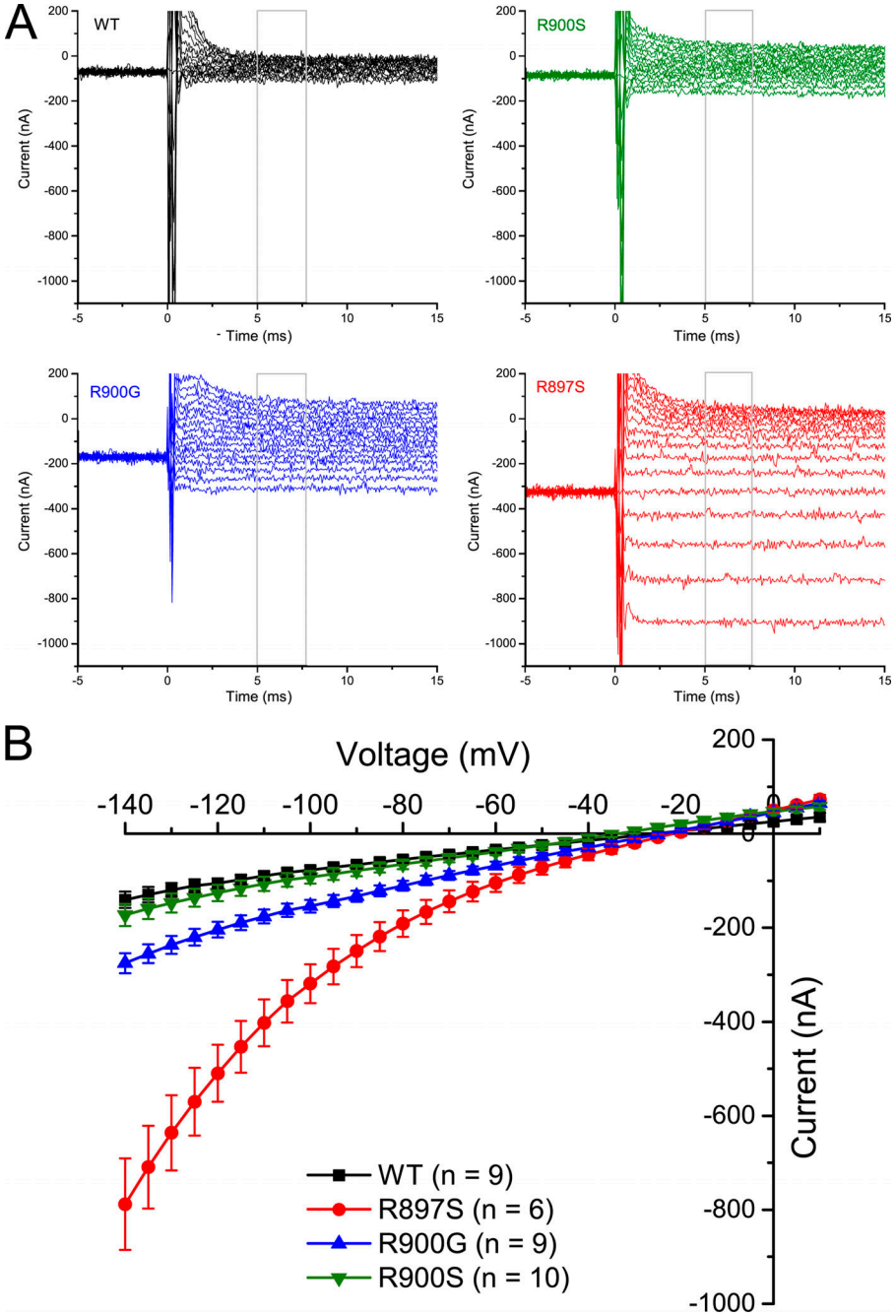

Figure 6. **Gating pore currents were detected for R897S and R900G, but not R900S, mutant channels. (A)** Representative traces are shown for currents recorded in response to test potentials of −140 to 20 mV in 10-mV increments from a holding potential of −100 mV. The initial capacitance transient is clipped, and the time-averaged current from 5 to 7.5 ms (boxes) was examined to test for the presence of a gating pore current. No leak subtraction was performed, and no hCa$_V$1.1 channel blockers were present. Notice the larger-amplitude inward holding current at −100 mV for R900G and R897S mutants. **(B)** The isochronal I-V relationship shows larger inward currents at hyperpolarized test potentials for R900G and R897S, consistent with a gating pore current. Error bars indicate the SEM.

R/H missense mutations), may be enhanced in extracellular guanidinium, and may be weakly blocked by multivalent cations (Sokolov et al., 2010; Starace and Bezanilla, 2004; Struyk and Cannon, 2007). Our initial measurements were performed in the context of the ion gradient for a normal mammalian cell, with Na^+ as the predominant extracellular cation and K^+ as the intracellular cation. Under these conditions, the reversal potential was approximately −20 mV (Fig. 6 B), consistent with a gating pore that is permeable to both Na^+ and K^+. The resting potential of skeletal muscle is substantially hyperpolarized (−90 mV) compared with the reversal potential of the gating pore, so, under physiological conditions, the predominant charge carrier would be an influx of Na^+.

The inward gating pore current is much larger in external guanidinium than for Na^+ with many S4 R/X HypoPP mutations in Na$_V$1.4 (Sokolov et al., 2010; Thor et al., 2019) and with the HypoPP Ca$_V$1.1-R528G mutation in DII (Wu et al., 2018). We assessed guanidinium permeability by initially recording the nonspecific leakage current in external NMDG and then repeated the measurement after exchanging the bath with a mixture of 60 mM guanidinium and 60 mM NMDG. Fig. 7 A (left panel) shows representative currents recorded from R897S-expressing oocytes in NMDG. Compared with the response in an Na^+ bath (Fig. 6, different R897S oocytes), the holding current at −100 mV is smaller, and the currents elicited over a range of voltage steps are more tightly clustered (i.e., lower

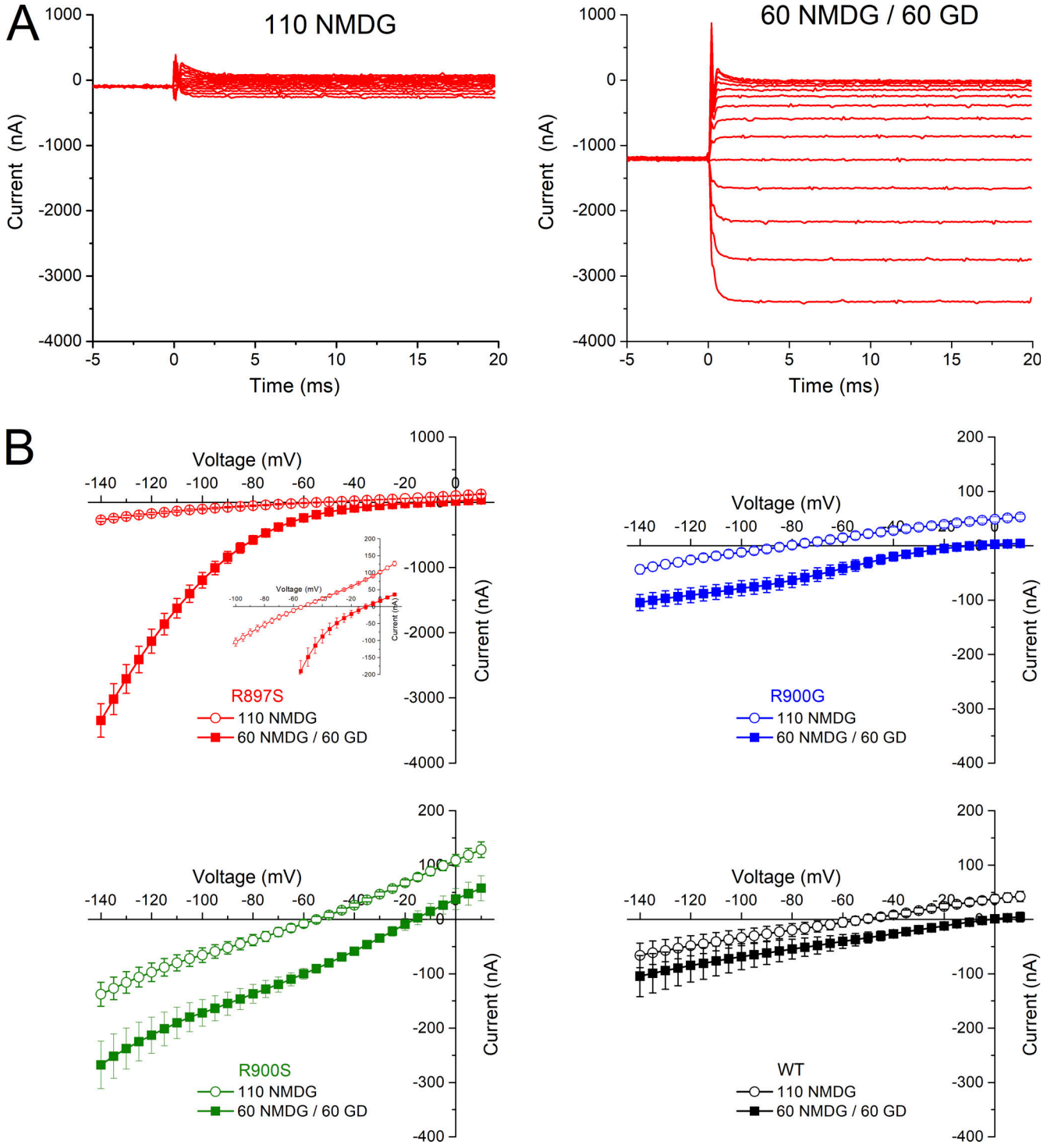

Figure 7. **Guanidinium is highly permeable for the R897S, but not the R900G, gating pore. (A)** Representative current traces were initially recorded in a 110 mM NMDG external solution (left) and recorded again from the same oocyte (right) after exchanging the external solution with a mixture of 60 mM NMDG and 60 mM guanidinium (GD). **(B)** The I-V relation is compared for a standard 96 mM Na^+ external solution and for a solution with a mixture of 60 mM guanidinium and 60 mM NMDG. Symbols show mean ± SEM (n = 3).

conductance) with little apparent inward rectification. These differences show that the R897S gating pore is much less permeable to NMDG than to Na^+. Moreover, this result also shows that R897S is not a proton-selective gating pore, because the currents have the same amplitude in Na^+ or NMDG for those HypoPP mutant channels (e.g., R667H and R669H in $Na_V1.4$; Struyk and Cannon, 2007; Struyk et al., 2008).

When the bath was exchanged from NMDG to a mixture of NMDG and guanidinium, the small ionic currents became very large and inwardly rectifying, as shown for the representative

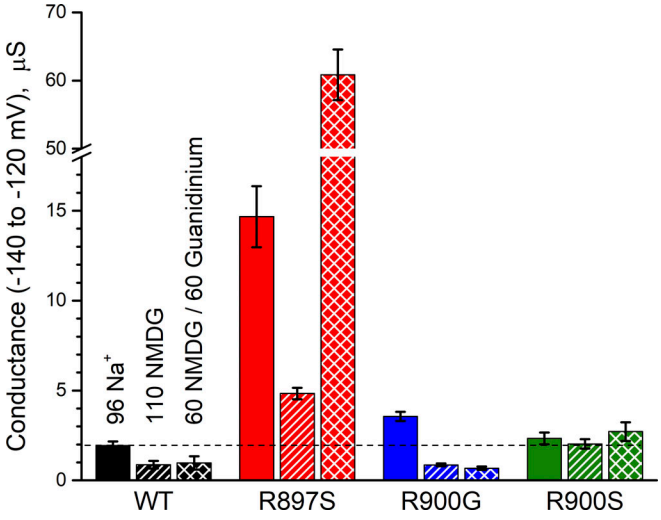

Figure 8. **Permeation properties of gating pore currents.** Each cluster of three bars shows the conductances measured in external Na^+, NMGD, or a mixture of 60 mM NMDG and 60 mM guanidinium. These conductance values were determined from the slope of the isochronal I-V over the range from −140 mV to −120 mV (e.g., Fig. 6 B for Na^+). Membrane conductance in Na^+ was higher for R897S and R900G than for WT, consistent with gating pore currents for these two HypoPP mutant channels. The marked decrease in conductance for R897S and R900G in NDMG compared with Na^+ shows that the gating pore is more permeable to Na^+ than NMDG. The conductance was increased in guanidinium only for R897S. The data for external Na^+ (n = 7 WT, 8 R897S, 9 R900G, and 10 R900S) are from a different set of oocytes than the NMDG/guanidinium studies. For the NMDG experiments (n = 5 WT, n = 3 for all mutants), recordings were initially made in 110 mM NMDG, and then the bath was exchanged with 60 mM NMDG plus 60 mM guanidinium, and currents were recorded again. Error bars indicate the SEM.

oocyte in Fig. 7 A (right panel). This dramatic change is strong supportive evidence for the presence of an anomalous gating pore conductance (Sokolov et al., 2010; Tombola et al., 2005), although not all gating pore conductances show this behavior (Wu et al., 2018). The average I-V response over the 5–8-ms isochronal interval is shown in Fig. 7 B for oocytes expressing WT and all three mutant constructs. Currents were recorded from each oocyte in NMDG, and then the same oocyte was tested with NMDG plus guanidinium. Only R897S oocytes had enhancement of the inwardly rectifying current in guanidinium (Fig. 7 B, upper left panel, red symbols). Although R900G showed clear evidence of a (nonrectifying) gating pore current in a Na^+ bath (Fig. 6), guanidium did not enhance the conductance (Fig. 7 B, upper right, blue symbols). In all oocytes, the reversal potential depolarized after the bath exchange (Fig. 7 B, open to closed symbol transition; see inset in upper left for E_{rev} of R897S), which implies that the small nonspecific leak was more permeable to guanidinium than to NMDG.

We calculated the slope of the isochronal I-V plots over the voltage range from −140 mV to −120 mV to quantitatively compare the membrane conductance for each $Ca_V1.1$ construct and how this changed for the different ionic conditions describe above. The slope conductances in Na^+, NMDG, and guanidinium are shown as a cluster of three bars for each construct in Fig. 8. In Na^+, the conductance was larger for the two HypoPP mutants with gating pore currents (R897S and R900G; $P < 0.0001$ and $P < 0.01$, respectively) than for WT or R900S. These larger conductances for R897S and R900G were both markedly reduced in external NMDG (lower by 9.8 µS for R897S and by 2.7 µS for R900G). By comparison, the conductance in NMDG was 1.1 µS lower for WT. The larger reductions of conductance in mutant channels (R897S and R900G) than in WT shows that the lower conductance in NDMG is caused primarily by an effect on the gating pore component of the current rather than by the nonspecific leakage current. These observations show that the gating pores are more permeable to Na^+ than to NMDG and imply that Na^+ influx is the major charge carrier of the gating pore current at the resting potential of skeletal muscle. The conductance in guanidinium is fourfold higher than in Na^+ for R897S. The other $Ca_V1.1$ constructs had either a conductance decrease (R900G and WT) or no change (R900S) in guanidinium.

Divalent block of the $Na_V1.4$ gating pore for mutant channels found in HypoPP is modest (K_d values of ∼0.5 to 3 mM) with block by $Ca^{2+} < Ba^{2+} < Ni^{2+} \approx Zn^{2+}$ (Francis et al., 2011; Sokolov et al., 2007). We assessed sensitivity to divalent block by comparison of the current in 6 mM Ca^{2+} (control) with the response in the same oocyte after bath exchange with 2 mM test divalent cation plus 4 mM Ca^{2+}. A total divalent of 6 mM was maintained to keep the effects of screening membrane surface charge relatively constant and to avoid the development of nonspecific leakage current in low divalent cation conditions. From the holding potential of −100 mV, 2 mM Ba^{2+} reduced the current at V_{step} −120 mV by 290 ± 41 nA in oocytes expressing R897S and by 83 ± 11 nA for R900G (Fig. 9, left column). Because the measured current is a combination of the gating pore and nonspecific leakage components, it is not possible to quantitatively estimate the potency of block. These data, however, are consistent with block of I_{gp} because, in oocytes expressing WT channels, 2 mM Ba^{2+} reduced the current at −120 mV by only 62 ± 5.1 nA. We also tested Co^{2+} because this divalent cation blocks the Ca^{2+}-conducting pore of $Ca_V1.1$ and thereby is potentially a good condition in which to record I_{gp} without interference from main pore currents. Application of 2 mM Co^{2+} to oocytes expressing R897S or R900G did not produce a detectable block of I_{gp}, as shown by the absence of an effect on the total current over the range −120 mV to 10 mV (Fig. 9, right column).

Discussion

This study is the first opportunity to ascertain whether the canonical HypoPP mutations in VSDIII of $Ca_V1.1$ (i.e., R/X substitutions in S4 that do not conserve charge) give rise to gating pore currents. These anomalous currents were clearly detected for two mutations (R897S and R900G), but not a third (R900S). The gating pore current is widely accepted as the primary defect that causes susceptibility to recurrent episodes of depolarization-induced loss of excitability and weakness in HypoPP (Cannon, 2015; Cannon, 2017). This anomalous current has been observed for six of eight HypoPP mutations that have been functionally studied with sufficient resolution to detect these small-amplitude currents (Table 3). In further support of this proposed pathomechanism, a gating pore current was detected for V876E

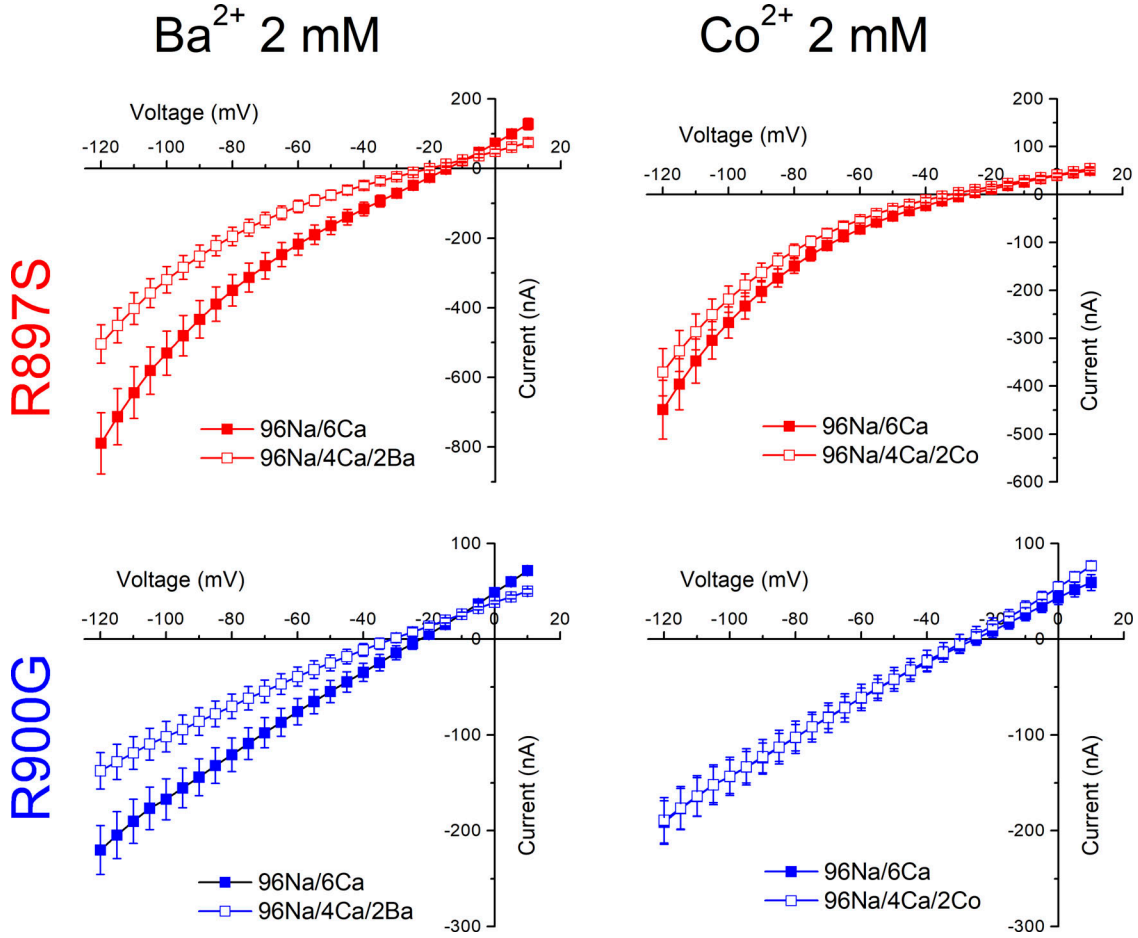

Figure 9. **Gating pore currents are partially blocked by Ba^{2+}.** Each panel shows the I-V relation, as in Fig. 3 B, recorded from oocytes in control conditions (96 mM Na^+, 6 mM Ca^{2+} external) and then with a 2 mM challenge using either Ba^{2+} or Co^{2+}. Current amplitude was reduced by Ba^{2+} but not Co^{2+}. Holding potential −100 mV with no leak subtraction. Symbols show mean ± SEM (n = 4 or 5 R900G; n = 5 or 10 R897S).

in DIII-S3, which is the only established HypoPP mutation that is not an R/X substitution in an S4 segment (Fuster et al., 2017b). Failure to detect a gating pore current for HypoPP mutant $Ca_V1.1$ channels has occurred twice: for an unusual mutation that preserves charge, R897K (Kubota et al., 2020), and for R900S in this study. Interestingly, gating pore currents are unequivocally detected for alternative missense changes at both of these same residues: R897S and R900G.

The gating pore currents observed for R897S are exceptional for two reasons. First, the magnitude of the current is larger than for I_{gp} recorded from any other HypoPP mutation of $Ca_V1.1$ or $Na_V1.4$ that has been studied in the oocyte expression system.

Table 3. **Functional assessment of HypoPP mutations in $Ca_V1.1$**

Domain	Mutation	Method	Gating pore current	References
II	R528H (R1)	Oocyte, knock-in mouse fiber, human fiber	Yes	Wu et al., 2018; Wu et al., 2012; Jurkat-Rott et al., 2009
	R528G (R1)	Oocyte	Yes	Wu et al., 2018
	R528C (R1)	Not done	?	
III	V876E (S3)	Mouse fiber (electroporation)	Yes	Fuster et al., 2017b
	R897K (R1)	Oocyte	No	Kubota et al., 2020
	R897S (R1)	Oocyte	Yes	This study
	R900G (R2)	Oocyte	Yes	This study
	R900S (R2)	Oocyte	No	This study
IV	R1239H (R2)	Mouse fiber (electroporation), human fiber	Yes	Fuster et al., 2017a; Jurkat-Rott et al., 2009
	R1239G (R2)	Not done	?	

The gating pore current for HypoPP mutant channels is typically 50–100 nA at −100 mV in 96 mM external Na^+ (Sokolov et al., 2007; Struyk and Cannon, 2007; Struyk et al., 2008; Wu et al., 2018). The gating pore current in R897S is approximately three times larger (Fig. 6). This pronounced biophysical defect correlates with the severe clinical phenotype in R897S patients and thereby supports the notion that the gating pore current is the critical functional defect underlying susceptibility to HypoPP. Two unrelated individuals with de novo R897S have been described in the literature, and both had severe HypoPP with hypotonia at birth, early onset of episodic weakness in infancy, daily attacks of weakness, secondary joint deformities, and progressive myopathy with difficulty walking distances independently as teenagers (Chabrier et al., 2008; Hanchard et al., 2013).

The other remarkable feature of I_{gp} for R897S is the pronounced inward rectification (Figs. 6 and 7). Inward rectification is usually a defining feature of the gating pore currents for Na_V or K_V channels with R/X missense mutations of the outer R1 and R2 arginines (Sokolov et al., 2007; Starace and Bezanilla, 2004; Struyk and Cannon, 2007; Tombola et al., 2005). This rectification, often "strong," occurs in symmetrical solutions of the permeant ion and has a voltage dependence similar to the gating charge displacement $Q(V)$, consistent with the model that rectification occurs as a result of outward motion of the S4 segment that closes the conduction pathway at depolarized potentials. The gating pore currents observed for $Ca_V1.1$ mutant channels are atypical in this regard. The $I_{gp} - V$ relation is approximately linear over a voltage range from −140 mV to 0 mV. This linear behavior for I_{gp} in HypoPP mutant $Ca_V1.1$ has been reported for R/X mutations in S4 of DII or DIV and for the atypical V876E in S3 expressed in oocytes (Wu et al., 2018) or mouse muscle fibers (Fuster et al., 2017a; Fuster et al., 2017b; Wu et al., 2012). R900G in DIII also has a linear I_{gp} (Fig. 6 B). We propose that I_{gp} is also inwardly rectifying for $Ca_V1.1$ channels with R/X mutations in the R1 and R2 positions, but the opportunity to observe this effect is obscured by the rightward shift of voltage-dependent activation of S4 segments (compared with $Na_V1.4$ channels) in combination with the interference from incompletely blocked ionic currents for $V > 10$ mV. For the cut-open oocyte preparation, these interfering currents include incomplete block of the $Ca_V1.1$ pore and outwardly rectifying endogenous currents activated for $V > 0$ mV. Recent evidence from voltage-clamp fluorometry shows the outward movement of the DIII-S4 is markedly leftward shifted compared with the DII-S4 ($V_{1/2}$ = −27 ± 1.1 mV compared with 4.6 ± 1.1 mV; Savalli et al., 2020). This leftward shift and R897S being in the R1 position could account for the observed rectification for this HypoPP mutation in $Ca_V1.1$, whereas $I_{gp} - V$ is approximately linear over the observable range of −140 mV to 0 mV for other HypoPP mutations because the voltage-dependent closure of the gating pore conductance is more depolarized for R2 (R900G) or for S4 in DII (R528H and R528G).

How can the failure to detect gating pore currents in the cut-open oocyte preparation for two HypoPP $Ca_V1.1$ mutations, R897K and R900S, be reconciled with the strong consensus that I_{gp} is the critical defect that predisposes a muscle fiber to paradoxical depolarization with hypokalemia, loss of excitability, and weakness? The first issue to be addressed is the confidence level with which these variants have been classified as pathogenic mutations that cause HypoPP. R897K was identified in three separate HypoPP pedigrees (one Japanese de novo; two French, with one inherited and the other de novo); the variant was not found in unaffected family members, and affected individuals had classical symptoms with recurrent episodes of weakness with low K^+ (<3 mM), episodes triggered by carbohydrate ingestion or rest after exercise, and improvement with oral K^+ supplementation and acetazolamide (Kubota et al., 2020). The R900S variant has been reported for an individual in the UK (Matthews et al., 2009) and for a family in Hangzhou, China (Ke et al., 2015). The clinical presentation was typical for HypoPP and included recurrent episodes of weakness associated with low K^+, attacks often occurring at night or upon awakening, attacks provoked by carbohydrate meals or rest after exercise, and onset in the second decade of life. In the Chinese family, two male cousins and their uncle were symptomatic, whereas three female carriers of R900S did not have any muscle symptoms. There is precedent for reduced penetrance of the phenotype with absence of transient attacks of weakness in females for the most commonly occurring HypoPP mutation, $Ca_V1.1$-R528H (Links et al., 1994). In these cases, however, the females usually develop slowly progressive permanent weakness that is detected during clinical examination by middle age. A grandmother in the R900S pedigree from China remains asymptomatic with no fixed weakness. Neither variant is present in the Genome Aggregation Database (gnomAD version 2.1) of 141,456 individuals. Taken together, these data support the interpretation that R897K and R900S are both likely to be pathogenic mutations for HypoPP.

Another possibility is that R897K and R900S both support gating pore currents, but the amplitude was below the detection limit of our measurements (two SD = ± 51 nA from the mean holding current of −77 nA at −100 mV for WT). It is reasonable to expect gating pore currents to be smaller for R900S than for R900G because of the greater steric hindrance from serine than from glycine. Similarly, the charge-conserving R897K would likely be accommodated better than R897S at the critical hydrophobic plug of the CTC in the VSD (Monteleone et al., 2017). On the other hand, simulations of the K^+ sensitivity for the resting potential of skeletal muscle show that a gating pore current with a magnitude less than half of that detected for R900G herein is not likely to cause susceptibility to paradoxical depolarization and weakness in low K^+ (Kubota et al., 2020). Alternatively, the gating pore current might be more prominent when these mutant channels are expressed in the context of a human muscle fiber instead of a frog oocyte. Finally, we should stay open-minded to the possibility of other mechanisms by which mutant $Ca_V1.1$ subunits may cause susceptibility to HypoPP. For example, the level of expression at the membrane is lower (smaller Q_{max} and G_{max}; Tables 1 and 2), and the kinetics of channel activation are slower (Fig. 3).

Acknowledgments

Jeanne M. Nerbonne served as editor.

The authors thank the members of the Olcese laboratory at the University of California, Los Angeles, for assistance with oocytes and M. DiFranco for technical assistance with the cut-open clamp.

This work was supported by the National Institutes of Health/National Institute of Arthritis and Musculoskeletal and Skin Diseases (R01-AR063182).

The authors declare no competing financial interests.

Author contributions: F. Wu and S. Cannon designed the experiments and analyzed the data. F. Wu performed the oocyte recordings, and M. Quinonez assisted with the molecular biology. S. Cannon wrote the paper, and all authors made revisions and approved the final version.

Submitted: 22 April 2021
Accepted: 12 August 2021

References

Cannon, S.C. 2015. Channelopathies of skeletal muscle excitability. *Compr. Physiol.* 5:761–790. https://doi.org/10.1002/cphy.c140062

Cannon, S.C. 2017. Sodium channelopathies of skeletal muscle. *Handb. Exp. Pharmacol.* 246:309–330. https://doi.org/10.1007/164_2017_52

Chabrier, S., N. Monnier, and J. Lunardi. 2008. Early onset of hypokalaemic periodic paralysis caused by a novel mutation of the CACNA1S gene. *J. Med. Genet.* 45:686–688. https://doi.org/10.1136/jmg.2008.059766

Francis, D.G., V. Rybalchenko, A. Struyk, and S.C. Cannon. 2011. Leaky sodium channels from voltage sensor mutations in periodic paralysis, but not paramyotonia. *Neurology.* 76:1635–1641. https://doi.org/10.1212/WNL.0b013e318219fb57

Fuster, C., J. Perrot, C. Berthier, V. Jacquemond, and B. Allard. 2017a. Elevated resting H^+ current in the R1239H type 1 hypokalaemic periodic paralysis mutated Ca^{2+} channel. *J. Physiol.* 595:6417–6428. https://doi.org/10.1113/JP274638

Fuster, C., J. Perrot, C. Berthier, V. Jacquemond, P. Charnet, and B. Allard. 2017b. Na leak with gating pore properties in hypokalemic periodic paralysis V876E mutant muscle Ca channel. *J. Gen. Physiol.* 149:1139–1148. https://doi.org/10.1085/jgp.201711834

Hanchard, N.A., D.R. Murdock, P.L. Magoulas, M. Bainbridge, D. Muzny, Y. Wu, M. Wang, J.R. Lupski, R.A. Gibbs, and C.W. Brown. 2013. Exploring the utility of whole-exome sequencing as a diagnostic tool in a child with atypical episodic muscle weakness. *Clin. Genet.* 83:457–461. https://doi.org/10.1111/j.1399-0004.2012.01951.x

Horstick, E.J., J.W. Linsley, J.J. Dowling, M.A. Hauser, K.K. McDonald, A. Ashley-Koch, L. Saint-Amant, A. Satish, W.W. Cui, W. Zhou, et al. 2013. Stac3 is a component of the excitation-contraction coupling machinery and mutated in Native American myopathy. *Nat. Commun.* 4:1952. https://doi.org/10.1038/ncomms2952

Jurkat-Rott, K., M.A. Weber, M. Fauler, X.H. Guo, B.D. Holzherr, A. Paczulla, N. Nordsborg, W. Joechle, and F. Lehmann-Horn. 2009. K^+-dependent paradoxical membrane depolarization and Na^+ overload, major and reversible contributors to weakness by ion channel leaks. *Proc. Natl. Acad. Sci. USA.* 106:4036–4041. https://doi.org/10.1073/pnas.0811277106

Jurkat-Rott, K., J. Groome, and F. Lehmann-Horn. 2012. Pathophysiological role of omega pore current in channelopathies. *Front. Pharmacol.* 3:112. https://doi.org/10.3389/fphar.2012.00112

Ke, Q., F. He, L. Lu, P. Yu, Y. Jiang, C. Weng, H. Huang, X. Yi, and M. Qi. 2015. The R900S mutation in CACNA1S associated with hypokalemic periodic paralysis. *Neuromuscul. Disord.* 25:955–958. https://doi.org/10.1016/j.nmd.2015.09.006

Kubota, T., F. Wu, S. Vicart, M. Nakaza, D. Sternberg, D. Watanabe, M. Furuta, Y. Kokunai, T. Abe, N. Kokubun, et al. 2020. Hypokalaemic periodic paralysis with a charge-retaining substitution in the voltage sensor. *Brain Commun.* 2:fcaa103. https://doi.org/10.1093/braincomms/fcaa103

Liman, E.R., J. Tytgat, and P. Hess. 1992. Subunit stoichiometry of a mammalian K^+ channel determined by construction of multimeric cDNAs. *Neuron.* 9:861–871. https://doi.org/10.1016/0896-6273(92)90239-A

Links, T.P., A.J. Smit, W.M. Molenaar, M.J. Zwarts, and H.J. Oosterhuis. 1994. Familial hypokalemic periodic paralysis. Clinical, diagnostic and therapeutic aspects. *J. Neurol. Sci.* 122:33–43. https://doi.org/10.1016/0022-510X(94)90049-3

Matthews, E., R. Labrum, M.G. Sweeney, R. Sud, A. Haworth, P.F. Chinnery, G. Meola, S. Schorge, D.M. Kullmann, M.B. Davis, and M.G. Hanna. 2009. Voltage sensor charge loss accounts for most cases of hypokalemic periodic paralysis. *Neurology.* 72:1544–1547. https://doi.org/10.1212/01.wnl.0000342387.65477.46

Mi, W., V. Rybalchenko, and S.C. Cannon. 2014. Disrupted coupling of gating charge displacement to Na^+ current activation for DIIS4 mutations in hypokalemic periodic paralysis. *J. Gen. Physiol.* 144:137–145. https://doi.org/10.1085/jgp.201411199

Monteleone, S., A. Lieb, A. Pinggera, G. Negro, J.E. Fuchs, F. Hofer, J. Striessnig, P. Tuluc, and K.R. Liedl. 2017. Mechanisms responsible for ω-pore currents in Ca_v calcium channel voltage-sensing domains. *Biophys. J.* 113:1485–1495. https://doi.org/10.1016/j.bpj.2017.08.010

Moreau, A., P. Gosselin-Badaroudine, and M. Chahine. 2014. Molecular biology and biophysical properties of ion channel gating pores. *Q. Rev. Biophys.* 47:364–388. https://doi.org/10.1017/S0033583514000109

Nelson, B.R., F. Wu, Y. Liu, D.M. Anderson, J. McAnally, W. Lin, S.C. Cannon, R. Bassel-Duby, and E.N. Olson. 2013. Skeletal muscle-specific T-tubule protein STAC3 mediates voltage-induced Ca^{2+} release and contractility. *Proc. Natl. Acad. Sci. USA.* 110:11881–11886. https://doi.org/10.1073/pnas.1310571110

Polster, A., S. Perni, H. Bichraoui, and K.G. Beam. 2015. Stac adaptor proteins regulate trafficking and function of muscle and neuronal L-type Ca^{2+} channels. *Proc. Natl. Acad. Sci. USA.* 112:602–606. https://doi.org/10.1073/pnas.1423113112

Savalli, N., M. Angelini, F. Steccanella, F. Wu, M. Quinonez, S.C. Cannon, and R. Olcese. 2020. The contribution of the individual voltage sensors to the activation of skeletal $Ca_V1.1$ channels [abstract]. *Biophys. J.* 118(3, Suppl 1):105a. https://doi.org/10.1016/j.bpj.2019.11.728

Sokolov, S., T. Scheuer, and W.A. Catterall. 2007. Gating pore current in an inherited ion channelopathy. *Nature.* 446:76–78. https://doi.org/10.1038/nature05598

Sokolov, S., T. Scheuer, and W.A. Catterall. 2010. Ion permeation and block of the gating pore in the voltage sensor of $Na_V1.4$ channels with hypokalemic periodic paralysis mutations. *J. Gen. Physiol.* 136:225–236. https://doi.org/10.1085/jgp.201010414

Starace, D.M., and F. Bezanilla. 2001. Histidine scanning mutagenesis of basic residues of the S4 segment of the shaker k^+ channel. *J. Gen. Physiol.* 117:469–490. https://doi.org/10.1085/jgp.117.5.469

Starace, D.M., and F. Bezanilla. 2004. A proton pore in a potassium channel voltage sensor reveals a focused electric field. *Nature.* 427:548–553. https://doi.org/10.1038/nature02270

Sternberg, D., T. Maisonobe, K. Jurkat-Rott, S. Nicole, E. Launay, D. Chauveau, N. Tabti, F. Lehmann-Horn, B. Hainque, and B. Fontaine. 2001. Hypokalaemic periodic paralysis type 2 caused by mutations at codon 672 in the muscle sodium channel gene SCN4A. *Brain.* 124:1091–1099. https://doi.org/10.1093/brain/124.6.1091

Struyk, A.F., and S.C. Cannon. 2007. A Na^+ channel mutation linked to hypokalemic periodic paralysis exposes a proton-selective gating pore. *J. Gen. Physiol.* 130:11–20. https://doi.org/10.1085/jgp.200709755

Struyk, A.F., and S.C. Cannon. 2008. Paradoxical depolarization of BA^{2+}-treated muscle exposed to low extracellular K^+: insights into resting potential abnormalities in hypokalemic paralysis. *Muscle Nerve.* 37:326–337. https://doi.org/10.1002/mus.20928

Struyk, A.F., V.S. Markin, D. Francis, and S.C. Cannon. 2008. Gating pore currents in DIIS4 mutations of $Na_V1.4$ associated with periodic paralysis: saturation of ion flux and implications for disease pathogenesis. *J. Gen. Physiol.* 132:447–464. https://doi.org/10.1085/jgp.200809967

Thor, M.G., V. Vivekanandam, M. Sampedro-Castañeda, S.V. Tan, K. Suetterlin, R. Sud, S. Durran, S. Schorge, D.M. Kullmann, M.G. Hanna, et al. 2019. Myotonia in a patient with a mutation in an S4 arginine residue associated with hypokalaemic periodic paralysis and a concomitant synonymous CLCN1 mutation. *Sci. Rep.* 9:17560. https://doi.org/10.1038/s41598-019-54041-0

Tombola, F., M.M. Pathak, and E.Y. Isacoff. 2005. Voltage-sensing arginines in a potassium channel permeate and occlude cation-selective pores. *Neuron.* 45:379–388. https://doi.org/10.1016/j.neuron.2004.12.047

Wu, F., W. Mi, E.O. Hernández-Ochoa, D.K. Burns, Y. Fu, H.F. Gray, A.F. Struyk, M.F. Schneider, and S.C. Cannon. 2012. A calcium channel mutant mouse model of hypokalemic periodic paralysis. *J. Clin. Invest.* 122:4580–4591. https://doi.org/10.1172/JCI66091

Wu, F., M. Quinonez, M. DiFranco, and S.C. Cannon. 2018. Stac3 enhances expression of human $Ca_V1.1$ in *Xenopus* oocytes and reveals gating pore currents in HypoPP mutant channels. *J. Gen. Physiol.* 150:475–489. https://doi.org/10.1085/jgp.201711962

Supplemental material

This text provides a numerical simulation to demonstrate the feasibility of estimating the gating charge displacement, based on conventional P/N leak-subtracted responses, despite the presence of a contribution from the nonlinear, voltage-dependent gating pore current. We previously showed that integration of current transients, for which a baseline correction was used to set the steady-state current equal to 0 nA at the end of a 10-ms voltage pulse, provides a reasonable estimate of gating charge displacement, $Q(V)$. More specifically, when the steady-state offset from the gating pore current was ∼5% of the peak current transient, then this correction to the integrated current produces an overestimate Q_{max} <8% (Mi et al., 2014).

For the R897S mutant of $Ca_V1.1$ studied herein, the gating pore current, I_{gp}, is much larger, with a magnitude comparable to the peak transient in the gating charge-displacement current, I_q. Because the gating pore is in a high-conductance state at hyperpolarized potentials, the conventional linear leak response measured from the holding potential (e.g., −100 mV) is an overestimate for the scaled P/N subtraction to be performed at a strongly depolarized test potential (e.g., +30 mV where the gating pore is nonconducting). The consequence of this inappropriately large subtraction is a pronounced negative shift of the steady-state current (Fig. 4 C). This problem for extracting the charge displacement (I_q) from the total current cannot be solved by choosing a different holding potential from which to measure passive leak response. Using a step from +30 mV to + 50 mV, for example, effectively removes the contribution of I_{gp} from the "passive linear leak" response. In order to measure the (off) gating charge movement, however, a large negative voltage step from +30 mV is required (e.g., to −80 mV), which will open the gating pore and produce an ionic current that will not be removed by P/N subtraction. In essence, any voltage change that is sufficient to move the gating charges will also change P_{open} of the gating pore and thereby cause an error with conventional P/N linear leak subtraction.

Modifications to the voltage-pulse protocol cannot be used to circumvent the problem of measuring charge displacement in the presence of a large-amplitude I_{gp}. Alternatively, we provide simulations that show our baseline correction to the P/N leak-subtracted current provides a reasonable estimate for $Q(V)$. As will be demonstrated with the simulations, the shape of the apparent $Q_{app}(V)$ implies the I_{gp} transient settles much faster than I_q, and therefore the gating pore current produces only modest distortion to the determination of Q. Importantly, even if this kinetic argument is relaxed, the distortion of $Q_{app}(V)$ does not cause a leftward (negative) shift of voltage dependence as was observed experimentally for R897S (Fig. 5 B).

The total current was simulated as a combination of a linear leak, I_{leak}; the nonlinear gating pore ionic current, I_{gp}; and the charge-displacement current, I_g. For a step change from V_1 to V_2 at $t = 0$:

$$I_{leak} = \begin{cases} G_{leak}(V_1 - E_{leak}) & for\ t < 0 \\ G_{leak}(V_2 - E_{leak}) & for\ t \geq 0 \end{cases}$$

$$I_{gp} = \begin{cases} G_{gp}g(V_1)(V_1 - E_{gp}) & for\ t < 0 \\ G_{gp}\{[g(V_2) - g(V_1)](1 - e^{-t/\tau_{gp}}) + g(V_1)\}(V_2 - E_{gp}) & for\ t \geq 0 \end{cases}$$

where $g(V) = 1/[1 + e^{(V - V_{gp})/k_{gp}}]$

$$I_q = \begin{cases} 0 & for\ t < 0 \\ \dfrac{Q(V_2) - Q(V_1)}{\tau_q} e^{-t/\tau_q} & for\ t \geq 0 \end{cases}$$

where $Q(V) = Q_{max}/[1 + e^{-(V - V_q)/k_q}]$.

The parameter values for maximum conductances, maximum gating charge, reversal potentials, and time constants are listed in Table S1. The relative speed of the transient currents (τ_{gp}/τ_q) is a critical determinant for how I_{gp} contributes to the error in estimating $Q(V)$. The smaller this ratio, the smaller the area will be for integrating the I_{gp} transient compared with I_q. In the limit of an instantaneous change in the gating pore conductance for an imposed ΔV, there will be no error in the determination of $Q(V)$ with P/N linear leak subtraction (after baseline current correction).

The anomalous ionic conductance of the gating pore occurs when the missense mutation resides in the hydrophobic waist of gating CTC (Monteleone et al., 2017), such that even a small local displacement of the S4 helix will ablate the conduction pathway. For this reason, we propose that the kinetics of the I_{gp} transient (regulated by a partial movement of the total gating charge) will be faster than the time course of I_q (which reflects displacement for all of the detectable gating charge). In our detailed simulations, we used $\tau_{gp}/\tau_q = 0.25$. Exploratory simulations were also performed for a wider range (0.1–1.0).

The total current (ionic plus charge displacement) is shown in Fig. S1 A for a series of voltage steps from a holding potential of −100 mV to values from −100 mV to +30 mV in 10-mV increments. No offset or leak subtraction has been performed. This simulation is comparable to the data recorded from an oocyte expressing R897S in Fig. 4 A. The contribution of individual current components is shown for $V_2 = +30$ mV in Fig. S1 B, which demonstrates the majority of the transient response is from I_q.

The response for each of the current components to our standard leak pulse −100 mV to −80 mV is shown in Fig. S1 C. Two nonlinear components in this leak response will contribute to errors in the linearly scaled P/N subtraction. First, there is a small gating charge-displacement current (magenta trace). Although the peak amplitude and corresponding area are small (18 nA and 0.008 nC, respectively, for a simulated Q_{max} = 0.3 nC), these components will be scaled up for subtraction; for example, 6.5-fold for a test pulse V_2 = +30 mV. The consequence is that $Q(V)$ will be slightly underestimated, and this error will increase linearly with more positive test potentials. This error of including some charge displacement in the P/N leak response produces a downsloping plateau to the $Q(V)$ curve at strongly depolarized potentials. The second error, and the major concern for this simulation, is the nonlinear current resulting from closure of the gating pore at positive test potentials. This effect is illustrated by the rapid transient (0–0.5 ms) that creates a "rounded shoulder" to the I_{gp} response (Fig. S1 C, blue line).

The consequences of linear P/N leak subtraction for the leak response in Fig. S1 C from the response to a test pulse of V_2 = 30 mV (Fig. S1 B) is shown in Fig. S1 D. The steady-state current at 5 ms is negative (approximately −600 nA, because the scaled leak response is too large) rather than the expected value of 0 nA for the isolated I_q current. This simulated response in Fig. S1 D is comparable to the P/N leak-subtracted data for an oocyte expressing R897S (Fig. 4 C, sweep in bold green). To correct for the steady-state nonlinear contribution of I_{gp}, we performed a secondary offset subtraction (i.e., after the P/N leak subtraction) to force the total steady-state current = 0 nA at the end of the fast transient. Fig. S1 E shows the effect of this correction for the P/N leak-subtracted current over the entire series of test potentials (V_2 = −100, −90, −80, ... + 30). The responses for these corrected traces at $t > 0$ ms have the expected amplitude and waveform of I_q and are comparable to the data obtained from R897S-injected oocytes (Fig. 4 D). The details of the contributions from the separate components of the current are shown for the case of V_2 = 30 mV in Fig. S1 F. Again, we see that the I_q transient (magenta line) is the major component of the transient for the total current (i.e., the experimentally measurable current; black line). The apparent charge displacement, Q_{app}, obtained by integrating the total current is 0.262 nC, which is nearly the same value as the true charge displacement (Q = 0.268 nC) calculated by integrating the isolated I_q trace. The shaded areas in Fig. S1 F show the P/N leak subtraction error contributed by I_{gp} (blue line), which causes $Q_{app} > Q$, and the P/N leak subtraction error contributed by the small I_q component in the leak response (green line), which causes $Q_{app} < Q$. In this case where τ_{gp}/τ_q = 0.25, the two errors tend to cancel, so $Q_{app} \approx Q$.

The critical influence of the ratio, τ_{gp}/τ_q, is illustrated by the $Q(V)$ curves calculated by integration of the simulated total current. Fig. S2 A shows a family of curves resulting from this ratio varying over the range of 0.1 to 1.0. The ideal simulated response, with no error contributed by I_{gp} or I_q in the leak response, is shown by the black squares. The other colors show cases for which the overestimate of $Q(V)$ becomes progressively worse as the ratio τ_{gp}/τ_q increases from 0.1 to 1.0 while the underestimate caused by including a small fraction of I_q in the leak response is held constant. The red squares correspond to the case of τ_{gp}/τ_q = 0.25 described in detail above. When the overestimate becomes more severe (e.g., τ_{gp}/τ_q = 0.5, orange line; or τ_{gp}/τ_q = 1.0, green line), the $Q(V)$ curve does not have a well-defined plateau and instead increases linearly with more positive test potentials. We did not observe this trend in the experimental data for R897S (Fig. 5 B), consistent with our proposal that $\tau_{gp} < \tau_q$. The solid curves in Fig. S2 A show the best fit of a Boltzmann function over the voltage range of −90 mV to +30 mV, as performed for the experimental data in Fig. 5 B. Based on the estimated value of Q_{app_max} from these fits, the data are amplitude normalized and replotted in Fig. S2 B. This scaled version facilitates a visual comparison of the voltage midpoint for charge displacement and shows that the error of $Q_{app}(V)$ from the contribution from the nonlinear I_{gp} transient in the leak pulse does not cause an apparent leftward shift. This simulation result supports our interpretation that R897S causes a substantial leftward shift of charge displacement (21 mV; Table 1) and is not an apparent shift created by an error from the contribution of I_{gp} to the P/N leak subtraction.

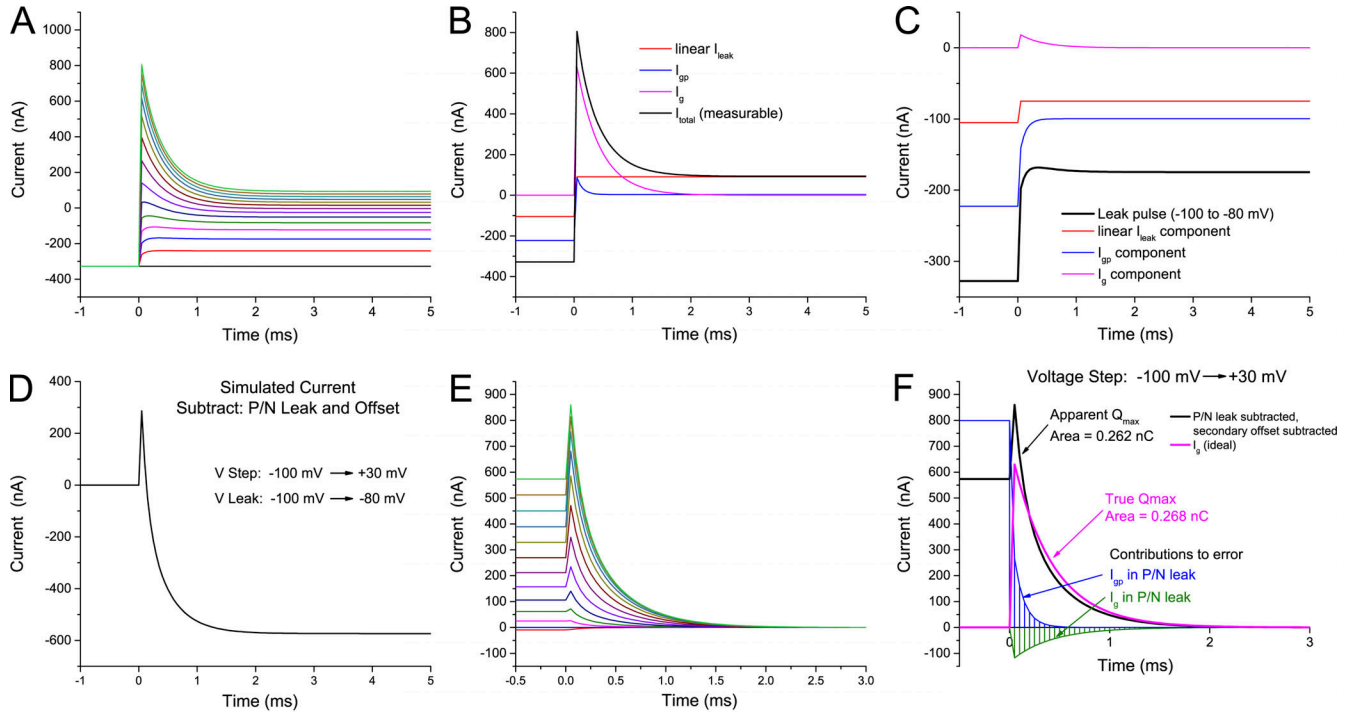

Figure S1. **Simulated currents produced by the sum of leak (I_{leak}), gating pore (I_{gp}), and charge-displacement components (I_q). (A)** Series of total currents elicited by step depolarization from a holding potential of −100 mV to a series of test potentials from −100 to +30 mV in 10-mV increments with no leak or offset subtraction. **(B)** Component currents that contribute to the response at +30 mV. **(C)** Leak response (black line) for a voltage step from −100 mV to −80 mV and the associated individual components. **(D)** Current response after standard P/N linear leak subtraction (and offset subtraction of the initial current $t < 0$) for the response to a voltage step V_2 = +30 mV. **(E)** Family of currents after secondary offset subtraction of the P/N-subtracted responses, such that the steady-state current = 0 nA. The applied voltage steps were over a range from −100 mV to +30 mV. **(F)** Details of the current components that contribute to the secondary offset-subtracted response at V_2 = +30 mV.

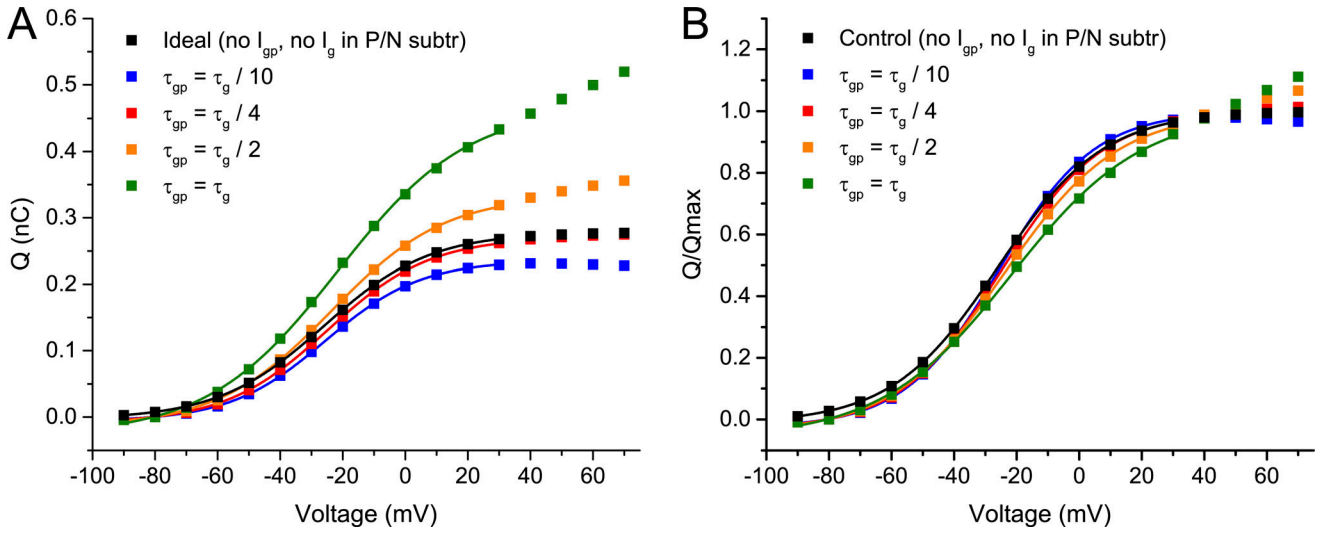

Figure S2. **Simulated $Q(V)$ curves. (A)** Family of $Q(V)$ curves when the ratio of τ_{gp}/τ_q was varied, as indicated in the legend. The black squares are for the idealized case with no contribution from I_{gp} or from the inclusion of a small I_q in the leak pulse. The solid lines show fits to a Boltzmann function over the range −90 mV to +30 mV. **(B)** Amplitude-normalized $Q(V)/Q_{max}$ responses from A to facilitate a visual comparison of the voltage midpoint for total charge displacement. subtr, subtraction.

Provided online is one table. Table S1 shows model parameters.